Lawrence Berkeley National Laboratory

Title
Microtopography of Electrochemical Surface Layers

Permalink
https://escholarship.org/uc/item/2282342f

Author
Muller, R.H.

Publication Date
1992

Lawrence Berkeley Laboratory
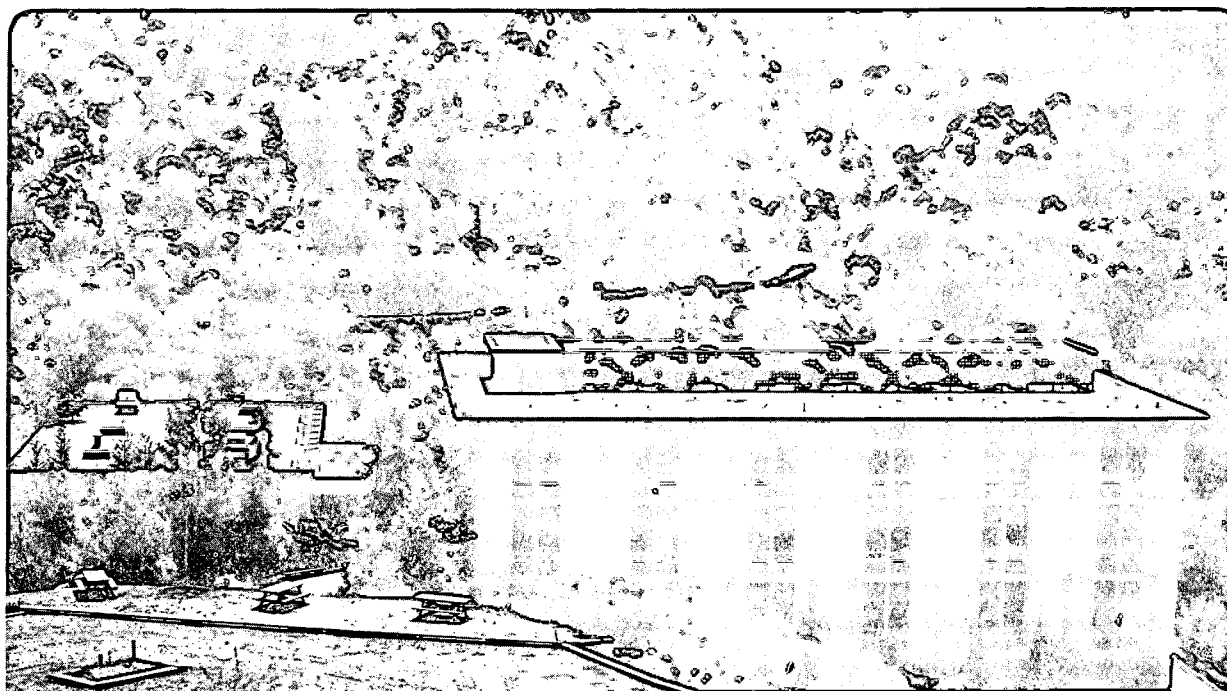## UNIVERSITY OF CALIFORNIA

Materials Sciences Division

To be published as a chapter in *New Trends and Approaches in Electrochemical Technology*, T. Osaka, N. Masuko, and Y. Fukunaka, Eds., Kodansha Scientific Limited of Tokyo and VCH of Weinheim, Germany, March 1992

Microtopography of Electrochemical Surface Layers

R.H. Muller

July 1991

DISCLAIMER

MICROTOPOGRAPHY OF
ELECTROCHEMICAL SURFACE LAYERS

Rolf H. Muller

Lawrence Berkeley Laboratory and
Department of Chemical Engineering,
University of California, Berkeley, CA 94720

Abstract

The microtopography of electrochemical surface layers has been investigated by spectroscopic ellipsometry, elastic light scattering, scanning tunneling microscopy, and Raman spectroscopy. From the measurements, conclusions on the mechanism of electrochemical film formation of copper-I and silver-I oxides and lead and copper metal have been drawn.

Introduction

The microtopography of surfaces is of interest for purposes of visual appearance and the control of optical properties needed in electro-optic applications. In addition, the topography of materials is often indicative of the underlying microstructure which, in turn, is related to many of its physical and chemical properties. For metal films, these properties include conductivity, porosity, reactivity, corrosion and wear resistance. The development of microtopography during the formation of surface layers also allows one to infer mechanisms of electrosolidification processes. Of particular interest here are the control of nucleation and growth of anodic and cathodic layers.

Since very thin layers, encountered in the early stages of film formation, are often not stable outside the electrolytic environment, the use of *in situ* experimental techniques is important for studies on the formation of electrochemical surface layers. Some of the principal techniques used are described briefly in the following section.

This report has been reproduced directly from the best available copy.

Experimental Techniques

Spectroscopic Ellipsometry

In ellipsometry, changes in the state of polarization, caused by the reflection of polarized light on the specimen surface, are measured. These measurements can be sensitive to changes in surface topography on the atomic scale, as they are to the formation of surface layers. In spectroscopic ellipsometry, measurements are conducted over a broad spectral range, thus greatly enhancing the information available for the interpretation of measurements in terms of physical quantities. The principles of ellipsometry, instrumentation and applications have been reviewed previously [1,2].

The ellipsometer used in this work is illustrated in Fig. 1 [3]. It has been upgraded in different ways since it was originally described [4]. It is of the compensating type that provides the greatest accuracy. The light beam propagates from the lower left to the upper right of the figure. It emanates from a Xe high-pressure white source. A narrow spectral band is selected by a rotating, continuously variable interference filter. A full spectral scan over the visible can be obtained in three sec. Telescopes are used to collimate and collect the beam. Faraday cells are located in the optical path before and after reflection on the specimen for modulation at 10 kHz and measurement by automatic compensation within about 1 ms. A Fresnel rhomb serves as achromatic compensator. The specimen is contained in the electrochemical cell shown in the center. The large amount of data generated during experiments is collected by a microcomputer.

Optical models are used for the interpretation of ellipsometer measurements. A large number of models has been investigated for their applicability to different electrochemical surface layers [5,6]; a few are illustrated in Fig. 2 [3]: In the simplest model, a layer is represented by a continuous, compact film on a smooth substrate. For known optical constants of film material and substrate, this model is defined by one parameter, the film thickness. The description of a single porous film of known composition requires two parameters, thickness and volume faction (porosity). Microroughness can often be represented by an equivalent porous layer. A new level of complexity is added to optical models by discontinuous or island films [7,8]. For known

2

optical properties of film and substrate materials such a model contains two unknown parameters, thickness and coverage. Multiple-layer models involve combinations of different types of single films. A model of this type that has been found applicable to silver oxide layers [9] employs islands of porous oxide (characterized by coverage, volume fraction, and thickness) on top of a nonporous oxide (characterized by thickness) and requires four parameters for its characterization. Inhomogeneous layers, in which optical properties change continuously with thickness, e.g., due to gradual changes in composition or porosity, can be represented by multiple layers; the results converge with increasing numbers of layers. This model requires only two parameters, the overall thickness and the functional dependence of the film properties on thickness. Linear and parabolic porosity profiles have been used [10]. Inhomogeneous films can also be used to represent surface roughness [11].

Optical models are selected under consideration of different experimental information, but primarily on the basis of their ability to predict ellipsometer measurements. In an optimization process, which usually requires a significant computational effort, the independent parameters of the model are systematically varied to achieve best agreement with measurements by minimizing the sum of squares difference between measured and predicted ellipsometer parameters [12]. With spectroscopic ellipsometer measurements, five-dimensional optimizations have been conducted [9]. Thus, five model parameters have been derived from the two ellipsometer parameters measured over the visible spectrum.

Elastic Light Scattering

The measurement of light scattered in different directions from an electrode surface at the incident wavelength (elastic scattering) has been used to obtain information on surface topography [13]. From the scattered intensity one can derive the number of scattering sites, from the angular distribution their size. The equipment built for this purpose is shown schematically in Fig. 3. A laser beam is incident normal (zero angle of incidence) on the electrode surface. The scattered light is collected over one quadrant by fiber optic probes from 5° to 85° in one degree increments. The fibers are selected sequentially by a rotating aperture and their light is directed to a photomultiplier.

Scanning Tunneling Microscopy

Scanning tunneling microscopy can provide surface topographic information with atomic resolution. A commercial instrument [14] has been used in this work in the constant tunneling-current (e.g., 2nA) mode of operation in which the probe tip is moved over the specimen surface with a constant tip-to-surface separation (e.g. 10 nm). For the observation of an immersed electrode, it has been found important to apply an insulating coating to the probe wire [15] in order to reduce the background current to values below the tunneling current (0.2 nA at 100 mV have been obtained). The probe tip is moved in three directions by a tube-shaped piezoelectric positioner. Depending on the cell design used, reference and counterelectrodes are located in the cell or connected to it by electrolyte-filled tubes.

The topographic (height) information obtained by scanning tunneling microscopy is collected in digital form and can be displayed in different ways. Four display modes used are illustrated in Fig. 4 for the same Cu deposit. The conventional line plot (upper left) shows a 600×450 nm area with 100 nm peak-to-valley distance. Contour lines with 18 nm increments are given in the upper right. The half-tone image on the lower left employs a height-coded gray scale with high regions being brighter than low regions. The image in the lower right employs a height-derivative coded gray scale. This display mode provides an image that is richest in surface detail.

Raman Spectroscopy

Raman spectroscopy has been used to provide vibrational spectra which are characteristic of the composition of electrode surfaces [16,17]. A highly efficient light collection system consisted of a single monochromator, used in conjunction with sharp band-pass interference filters for removing elastically scattered light and plasma lines from the laser. Also, the entire spectrum is observed simultaneously with a 1024 element intensified photodiode array connected to an optical multichannel analyzer. The electrochemical cell was equipped with windows for optimum angles of incidence (70° from the surface normal) and collection (60° from the surface normal and in the plane perpendicular to the plane of incidence).

4

The information obtained by use of the different techniques will be illustrated by results from two anodic and two cathodic systems.

Anodic Films

<u>Oxidation of Copper</u>

Spectroscopic ellipsometer measurements of the anodic formation of Cu_2O are illustrated in Fig. 5, where the measured phase parameter delta is shown as a function of potential and wavelength [13]. The potential sweep in the anodic direction extends from –600 mV to –300 mV and is followed by a cathodic sweep from –300 mV to – 900 mV. The data show the oxidation and reduction of the surface, with a maximum Cu_2O thickness (140 Å) being obtained at about –460 mV. Reversal of the potential sweep at –300 mV results in a small shelf in the plot. The wavelength-dependence of the data shows the spectral features of Cu and Cu_2O.

The cyclic voltammogram [13] corresponding to the optical measurements in Fig. 5 is given in Fig. 6. The anodic peak at –365 mV corresponds to the formation of Cu_2O [16]. The film thickness for the same specimen, also shown in Fig. 5, has been derived from the spectroscopic ellipsometer measurements. The thickness increases in the anodic region (even after reversal of the potential sweep direction) and decreases in the cathodic current region. The fastest decrease in thickness coincides with the cathodic current peak. The apparent negative thickness given below –700 mV is an artifact of the optical model used, which was that of a homogeneous single film and did not consider the roughening of the surface. The amount of oxide derived from the film thickness agrees with that expected from the charge passed.

The elastic light scattering during anodic oxidation of copper is illustrated in Fig. 7 for a larger range of potentials [13]. The scattering intensity increases with increasing anodic potential (–500 to –100 mV) in two steps which correspond to the formation of Cu_2O and $Cu(OH)_2$. The increase in scattering intensity is indicative of an increase in the number of scattering centers (roughness elements). The scattered light is distributed over all angles with an approximately $\cos^2$ dependence, which is characteristic for scattering from small particles. The light scattering results

are in agreement with results obtained by ellipsometry, scanning electron microscopy (SEM) and Raman spectroscopy.

From the spectral power density of the scattering [13] and an assumed initial roughness (100 Å), the RMS roughness of the copper electrode during oxidation has been derived from the light scattering measurements (Fig. 8). A small increase in roughness (about 200 Å) is observed during Cu_2O formation, supporting a solid-state transformation mechanism. The larger increase in roughness during $Cu(OH)_2$ formation at more anodic potentials agrees with a precipitation reaction for this product. Needles of precipitated hydroxide with about 600 Å diameter are shown in the SEM pictures of Fig. 9 [13], confirming the small dimensions derived from the scattering. The Cu_2O surface was found featureless by SEM.

Oxidation products on copper have been identified by Raman spectroscopy. Fig. 10 illustrates how, with increasing anodic (positive) potential, Cu_2O (633 cm^{-1}) is formed first, followed by $Cu(OH)_2$ (488 cm^{-1}) [16]. Since CuO is a weak Raman scatterer, its formation is not seen on the spectra. Its presence has been identified by modulated photoelectrochemical measurements [17]. Upon reversal of the potential sweep, the two Raman peaks disappear in reverse order.

Oxidation of Silver

The optical model that was found to best represent ellipsometer measurements of Ag_2O formation is shown in Fig. 11 [9]. It is a two-layer island film model that consists of a primary compact (nonporous), homogeneous oxide layer and a layer of porous secondary oxide crystals, represented by an island film. With the optical constants of Ag_2O being known, this model requires four parameters for its description: the thickness of the primary (compact) film and the porosity, thickness and coverage of the secondary (island) film. The two thickness parameters, derived from spectroscopic ellipsometer measurements for film growth at constant potential (above the nucleation potential) are given in Fig. 12 [9]. The primary layer is seen to grow initially from underpotential and monolayer to multilayer dimensions. Its thickness decreases greatly when the secondary crystals are nucleated (50 sec) and gradually recovers afterwards. The nucleation of the

secondary crystals is not immediate, although the applied potential is sufficient for nucleation. The induction time indicates the need for a critical primary layer thickness before nucleation. Such behavior is not expected on the basis of a dissolution-precipitation mechanism. The surface coverage by the secondary (island) film derived from the ellipsometer measurements, surprisingly, is found to decrease after nucleation. From thickness and coverage of the secondary layer, the number density of growing crystals has been derived (under the assumption of hemispherical shapes). This number density is found to decrease by several orders of magnitude during the early stages of film growth. For the galvanostatic conditions shown in Fig. 13, the number density decreases from 2×10^{10} cm^{-2} to 3×10^{8} cm^{-2} between 60 sec and 160 sec of film growth [9].

Light scattering measurements during Ag_2O formation are in agreement with the ellipsometer interpretation. As shown in Fig. 14, the angular distribution of scattered light changes during film growth from one over large angles from the incident (normal) direction, characteristic of small particles, to one over near angles, characteristic of large particles [13]. This change supports a redistribution of material between growth centers after nucleation of the secondary layer (at approximately 50 sec).

Scanning tunneling microscopy (STM) further confirms this redistribution : Fig. 15 shows a surface element of 2.3×3.06 μm in size [13]. The original substrate surface (A) is found to roughen gradually as the underpotential oxide layer grows to the primary multilayer (B). Nucleation of the secondary layer results in a sharp increase in roughness (C); about 2×10^{10} cm^{-2} peaks can be identified. The redistribution of oxide materials is seen in the remaining parts of Fig. 15, with the number of peaks counted as 5.7×10^{9} cm^{-2} in (E) and 2.8×10^{8} cm^{-2} in (F). The latter number compares well with 3×10^{8} cm^{-2} derived from earlier ellipsometer measurements (Fig. 13).

A proposed sequence of events in the anodic formation of Ag_2O that is in agreement with the different experimental observations is illustrated in Fig. 16 [9]: An initial monolayer (a), formed by adsorption and precipitation of dissolution products (c), grows to the primary multilayer

(b). Nucleation of the secondary crystal layer (d) occurs after the primary layer reaches a critical thickness (approximately 150 Å). The secondary crystals initially grow by the transfer of oxide from the primary layer (e), resulting in a decreased thickness of the latter. A further redistribution of oxide from small to large secondary crystals (f) results in a large decrease in the number density of secondary crystals. After the secondary crystals reach a diameter of about 1000 Å, their solubility does not depend greatly on size anymore and they continue to grow independently (g) in constant numbers. Also, the primary layer is reestablished (h).

Cathodic Films

Deposition of Lead

The initial stages in the deposition of lead on silver have been investigated by scanning tunneling microscopy (STM) [18]. The STM line scans in Fig. 17 show the initial roughening of the originally smooth, evaporated silver substrate by the formation of lead nuclei (A). Upon further deposition, the short-range roughness decreases (B). Subsequently, the deposit passes through several roughening (C) and smoothing (D) cycles with renucleation in recessed regions.

For the quantitative characterization of the surface topography of STM measurements, the amplitude density functions of the surfaces shown in Fig. 17 have been determined [13,18]. They are given in Fig. 18 and represent the probability of the presence of any height below (negative) or above (positive) the mean electrode surface. The original substrate (A) shows a narrow distribution of heights characteristic of smooth surfaces. The wide distribution given in Fig. 18B demonstrates the roughening seen in the corresponding Fig. 17A. The peak of the original distribution has been shifted to about –400 Å by the nucleation that causes the appearance of protrusions, shown on the positive side of the distribution. The repeated smoothing and roughening cycles are well visible in Figs. 18C to E, that correspond to Figs. 17B to D. The dual-mode distribution in Fig. 18D shows the recesses on the negative side of the distribution and the protrusions on the positive side.

8

As another evaluation of surface profiles, autocorrelation functions for the same surfaces are given in Fig. 19 [18]. The autocorrelation function for zero lag distance, which represents the square of the RMS roughness, shows the repeated changes from rough to smooth surfaces with corresponding large and small correlation distances, which correspond to the size of the surface features .

The observations are consistent with a deposition mechanism that involves the successive re-nucleation of growth centers in the thermodynamically favored recessed regions of the surface. As the growth exceeds the depth of the recesses, new roughness is generated.

Deposition of Copper

The effect of the brightening agent benzotriazole on the microtopography of electro-deposited copper has been investigated by STM [19,20]. Fig. 20 shows a derivative-coded gray scale STM image of Cu deposited from an acidic sulfate electrolyte in the absence of the brightening agent. In the active areas, large crystals with well-developed planar crystal facets (approximately 200 nm wide), resulting from the growth of a small number of nuclei, are formed. Between the active areas, large electrode regions (not shown) remained bare.

Under potential control (–50 mV vs. Cu) the deposit microtopography has been found to be stable after exhaustion of the dissolved copper, with atomically smooth regions separated by single- and multiatomic steps [15]. At open circuit, however, rapid dissolution started immediately, resulting in a loss of steps, thus illustrating the importance of *in situ* observation.

In the presence of benzotriazole [19], deposition occurs at a higher overpotential and results in a large number (approximately 9×10^{10} cm^{-2}) of uniformly distributed growth centers, which are considerably smaller (approximately 30 nm) than the wavelength of light (approximately 550 nm) (Fig. 21). Brightening is therefore achieved by the high nucleation density that results in small surface features.

Conclusions

The combination of different experimental techniques has been found useful for the study of electrochemical film formation. Physical mechanisms of film formation have been derived from the observed microtopographies. Similarities have been found in the nucleation and growth of anodic and cathodic surface layers. Approaches to the control of film properties can be based on the mechanisms of electrosolidification.

Acknowledgements

References

1. R. H. Muller, "Principles of Ellipsometry," in <u>Advances in Electrochemistry and Electrochemical Engineering</u>, Vol. 9, R. H. Muller, ed., pp. 167-226, Wiley, New York, 1973.

2. R. H. Muller, "Ellipsometry as an In Situ Probe for the Study of Electrode Processes," in <u>Techniques for Characterization of Electrodes and Electrochemical Processes</u>, R. Varma and J. R. Selman, eds., Wiley, New York, 1991.

3. S. T. Mayer, An Ellipsometric Spectroscopy Study of Anodically Formed Silver(I) Oxide Films on Silver, M.S. Thesis, University of California, Berkeley, Department of Chem. Engr. (Dec. 1985), Report LBL-20503.

4. R. H. Muller and J. C. Farmer, Fast Self-Compensating Spectral-Scanning Ellipsometer, Rev. Sci. Instrum. 55, 371-374 (1984).

5. R. H. Muller and C. G. Smith, Use of Film-Formation Models for the Interpretation of Ellipsometer Observations, Surf. Sci. 96, 375-400 (1980).

6. J. C. Farmer and R. H. Muller, Effect of Rhodamine-B on the Electrodeposition of Lead on Copper, J. Electrochem. Soc. 132, 313-319 (1985).

7. R. H. Muller and J. C. Farmer, Macroscopic Optical Model for the Ellipsometry of an Underpotential Deposit: Lead on Copper and Silver, Surf. Sci. 135, 521-531 (1983).

8. M. J. Armstrong and R. H. Muller, Island Films Resulting from Ion Bombardment: Spectroscopic Ellipsometry and Auger Electron Spectroscopy, J. Appl. Phys. 65, 3056-3060 (1989).

9. S. T. Mayer and R. H. Muller, Nucleation of Silver (I) Oxide Investigated by Spectroscopic Ellipsometry, J. Electrochem. Soc. 135, 2133-2142 (1988).

10. F. Schwager, Y. Geronov, and R. H. Muller, Ellipsometer Studies of Surface Layers on Lithium, J. Electrochem. Soc. 132, 285-289 (1985).

11. C. A. Fenstermaker and F. L. McCrackin, Errors Arising from Surface Roughness in Ellipsometric Measurement of the Refractive Index of a Surface, Surf. Sci. 16, 85-96 (1969).

12. J. C. Farmer and R. H. Muller, Nucleation of Pb Electrodeposits on Ag and Cu, J. Electrochem. Soc. 132, 39-45 (1985).

13. S. T. Mayer, An In Situ Study of the Anodic Film Formation of Cu, Ag, and Zn in Alkaline Media, Ph.D. dissertation, University of California, Berkeley, Dept. of Chem Engr. (Dec. 1989), Report LBL-28085.

14. Nanoscope I, Digital Instruments Inc., Goleta, CA 93117, U.S.A.

15. M. J. Armstrong and R. H. Muller, STM Observations of Electrodeposited Copper under Potential Control and Open Circuit, J. Electrochem. Soc. 136, 584-585 (1989).

16. S. T. Mayer and R. H. Muller, An In Situ Raman Spectroscopy Study of the Anodic Oxidation of Copper in Alkaline Media, J. Electrochem. Soc., in print.

17. D. T. Schwartz and R. H. Muller, Oxidation Films on Copper in Alkaline Media: Intensity-Modulated Photoelectrochemical and Raman Spectroscopy Studies, Surf. Sci. <u>248</u>, 349-358 (1991).

18. S. T. Mayer, R. H. Muller, and P. N. Ross, In Situ Scanning Tunneling Microscopy of Multilayer Pb Electrodeposition on Ag, ECS Meeting, Los Angeles, May 7-14, 1989, ext. abstr. No.521.

19. M. J. Armstrong and R. H. Muller, In Situ Scanning Tunneling Microscopy of Copper Deposition with Benzotriazole, J. Electrochem Soc., in print.

20. M. J. Armstrong, The Role of Inhibitors during Electrodeposition of Thin Metallic Films, Ph.D. dissertation, University of California, Berkeley, Dept. of Chem. Engr. (1990), Report LBL-28972.

Figure Captions

Fig. 1   (CBB 858-7021)
Self-compensating spectroscopic ellipsometer with white light source, rotating continuously variable interference filter, collimator with polarizer, first Faraday cell, achromatic compensator, specimen, second Faraday cell and (not visible) telescope with analyzer and photomultiplier.

Fig. 2   (XBL 8511-11509A)
Optical film models for the interpretation of spectroscopic ellipsometer measurements. For known optical constants of substrate and film materials, the number of unknown parameters increases with the complexity of the model from 1 to 4.

Fig. 3   (XBL 917-1405)
Schematic of scatterometer for the *in situ* measurement of elastically scattered light from an electrode surface as a function of scattering angle. The scattered light is collected in 1° increments by optical fibers (4 only shown for clarity) that are selected by a rotating aperture for sequential readout.

Fig. 4   (XBB 898-6773)
Display modes for STM topographic information. Cu deposit from 10 mM $Cu(ClO_4)_2$, 0.5 M $NaClO_4$, pH 2, 60 sec at -25 mV, after 30 sec at -500 mV. 600×450 nm area; line plot (110 nm peak-to-valley), contour lines (18 nm increments), height-coded gray scale, height-derivative coded gray scale.

Fig. 5   (XBL 888-8536)
Spectroscopic ellipsometer measurement (phase parameter delta) of oxidation and reduction of Cu (111) in 1 M KOH during potential sweep at 0.5 mV/s from -600 to -300 mV vs. Hg/HgO and back to -900 mV. Formation and reduction of 14 nm thick Cu_2O. Spectral features of Cu and Cu_2O are visible.

Fig. 6   (XBL 899-3374)
Formation and reduction of Cu_2O on Cu (111) in 1 M KOH. Current and thickness during potential sweep at 0.5 mV/s. Film thickness derived from spectroscopic ellipsometer measurements (delta shown in Fig. 5) by use of a single-film optical model with adjustable, wavelength-dependent optical constants; negative thickness due to roughening. Small persistent cathodic current due to oxygen reduction.

Fig. 7   (XBL 888-8535)
Elastic light scattering during anodic oxidation of Cu (111) in 1 M KOH. Potential sweep at 0.5 mV/s from -500 to -150 mV vs. Hg/HgO. Formation of Cu_2O and $Cu(OH)_2$. Small particles result in scattering over large angles. Scattering intensity background-subtracted, each angular scan is average of 30 scans acquired over 25 sec.

Fig. 8   (XBL 888-3086A)
Surface roughness during anodic oxidation of Cu derived from elastic light scattering at 0.5 mV/s shown in Fig. 7. Onset of Cu_2O formation at -400 mV, small nuclei; onset of $Cu(OH)_2$ formation at -200 mV, needles of 60 nm diameter.

Fig. 9   (XBB 879-8192)
Scanning electron micrograph of anodic $Cu(OH)_2$ layer formed at 100 mV vs. Hg/HgO in 1 M KOH showing precipitate needles of 60 nm diameter. Magnification shown holds for picture on left, scale bar 6450 nm; magnification 10 times higher at right, scale bar 645 nm.

13

Fig. 10   (XBL 891-348)
Raman spectroscopy of Cu oxidation in 1 M KOH. Anodic potential sweep at 0.5 mV/s. Spectra shown at selected potentials vs. Hg/HgO, offset for readability. Peaks at 488 cm^{-1} and 633 cm^{-1} for $Cu(OH)_2$ and Cu_2O, respectively. Detector exposure time 100 s/scan.

Fig. 11   (XBL 865-2106)
Two-layer island-film optical model for anodic Ag_2O formed on Ag (111) in 1 M KOH. Nonporous homogeneous (primary) layer and porous (secondary) oxide crystals represented by island film. Free parameters of model: thickness of nonporous layer and thickness, porosity and coverage of island layer.

Fig. 12   (XBL 876-3024)
Thickness of nonporous (primary) and porous island (secondary) oxide layers derived from spectroscopic ellipsometer measurements. Anodic oxidation of Ag (111) in 1 M KOH at 200 mV vs. Ag/AgCl, 4M KCl. Decrease of nonporous layer thickness at onset of island film growth.

Fig. 13   (XCG 8512-544)
Anodic oxidation of Ag (111) in 1 M KOH at 0.1 mA/cm^2. Number density of secondary oxide crystals derived from spectroscopic ellipsometer measurements. Decrease during early film growth stage indicates redistribution of oxide.

Fig. 14   (XBL 888-2935)
Elastic light scattering during anodic oxidation of Ag (111) in 1 M KOH at 200 mV vs. Hg/HgO. Formation of Ag_2O. Initial formation of many small particles results in scattering over large angles. Later redistribution of oxide to fewer large particles accounts for brief decrease in scattering intensity and scattering primarily over near angles. Scattering intensity background-subtracted, each angular scan is average of 4 scans acquired over 3.9 sec.

Fig. 15   (XBL 891-85)
Scanning tunneling micrographs of the anodic oxidation of sputtered Ag in 1 M KOH at 290 mV vs. Hg/HgO. After nucleation of secondary crystals in C, the number density of peaks decreases as their size increases.

Fig. 16   (XBL 876-3025)
Schematic representation of proposed film formation mechanism for Ag_2O on Ag in KOH. Formation of primary multilayer (b) from initial monolayer (a) and formation of soluble oxide species (c); nucleation of secondary crystals (d) that grow by transfer of oxide from primary layer (e) and small crystals (f); reestablishment of primary layer (h) at end.

Fig. 17   (XBL 891-75)
Scanning tunneling micrographs of different stages in the electrodeposition of Pb on Ag at –650 mV vs. Ag/AgCl from 5 mM PbAc, 1 M NaAc. Substrate surface featureless. (A) After 100 sec, bulk deposition with large number of small (5-10 nm) growth centers. (B) After 300 sec, reduction of short-range roughness by growth. (C) After 1000 sec, increase in roughness by nucleation in surface recesses. (D) After 1200 sec, reduction of roughness.

Fig. 18   (XBL 891-76)
Amplitude density function for Ag substrate surface (A) and Pb deposits (B-D) shown in Fig. 17. Successive roughening and smoothing cycles shown by broadening and narrowing of distribution.

Fig. 19   (XBL 891-77)
Autoconclation function for Pb deposits shown in Fig. 17. ■ 100 sec, ❑ 300 sec, ● 1000 sec, ○ 1200 sec. Successive roughening and smoothing cycles shown by value of autoconclation function at zero lag distance (square of RMS roughness).

Fig. 20   (XBB 894-3044)
Derivative-coded gray scale STM image of Cu deposited on Pt from 0.5 M $CuSO_4$, 0.5 M H_2SO_4 at –50 mV vs. Cu. Small number of large crystals with planar facets.

Fig. 21   (XBB 894-3045)
Derivative-coded gray scale STM image of Cu deposited on Pt from 0.5 M $CuSO_4$, 0.5 M H_2SO_4, 0.1 mM BTA. Large number of small growth centers.

Fig. 1
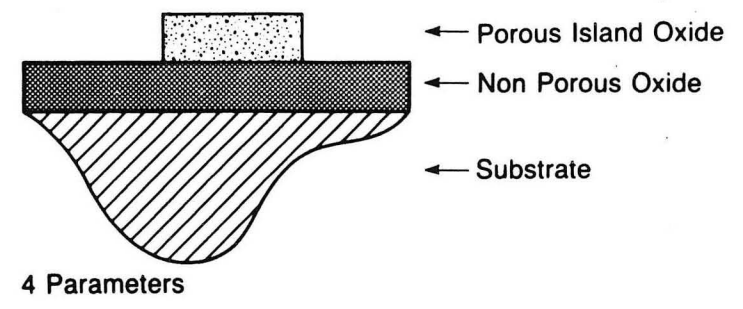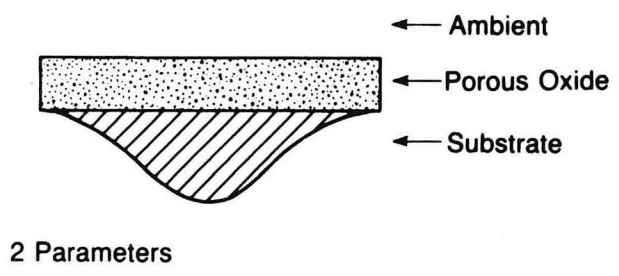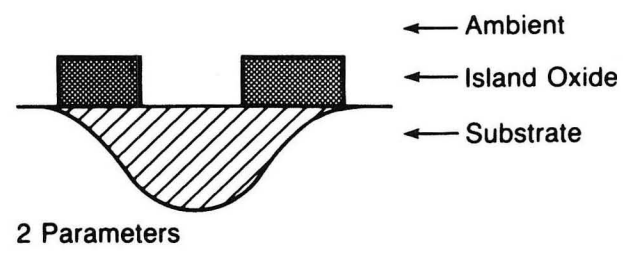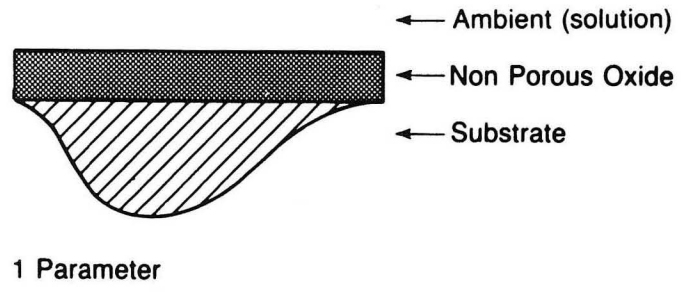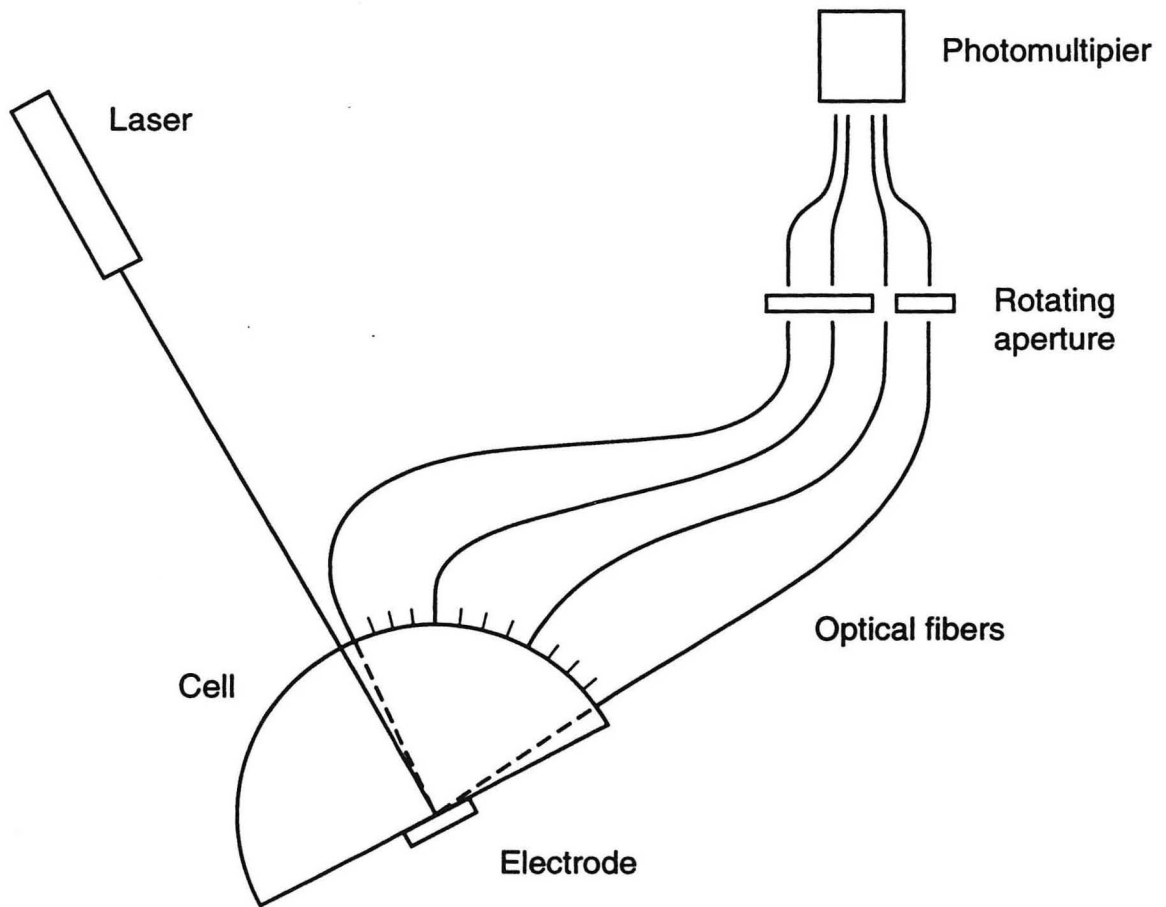
16

← Ambient (solution)
← Non Porous Oxide
← Substrate

1 Parameter

← Ambient
← Island Oxide
← Substrate

2 Parameters

← Ambient
← Porous Oxide
← Substrate

2 Parameters

← Porous Island Oxide
← Non Porous Oxide
← Substrate

4 Parameters

XBL 8511-11509A

Fig. 2

Laser

Photomultipier

Rotating
aperture

Optical fibers

Cell

Electrode

XBL 917-1405

Fig. 3

18

Fig. 4

19

Fig. 5

XBL 888-8536

XBL 899-3374

Fig. 6

21

XBL 888-8535

Fig. 7

22
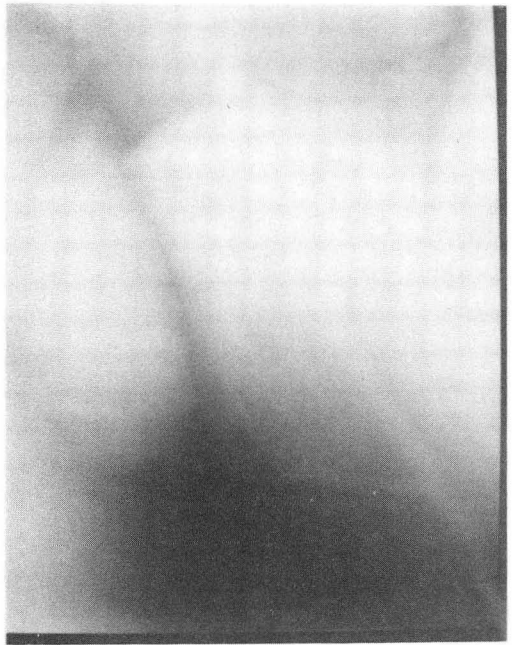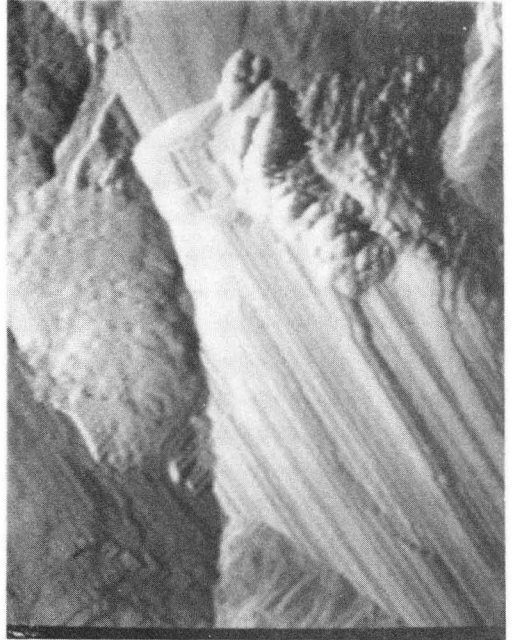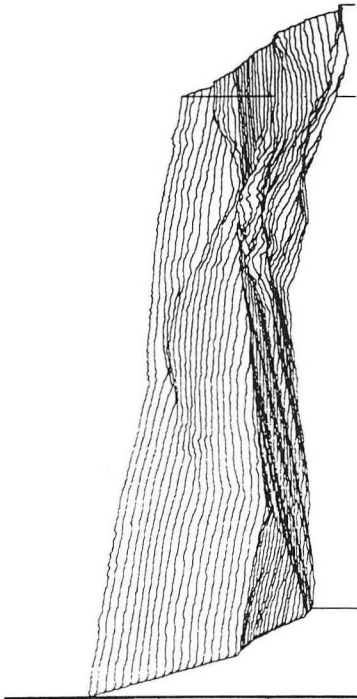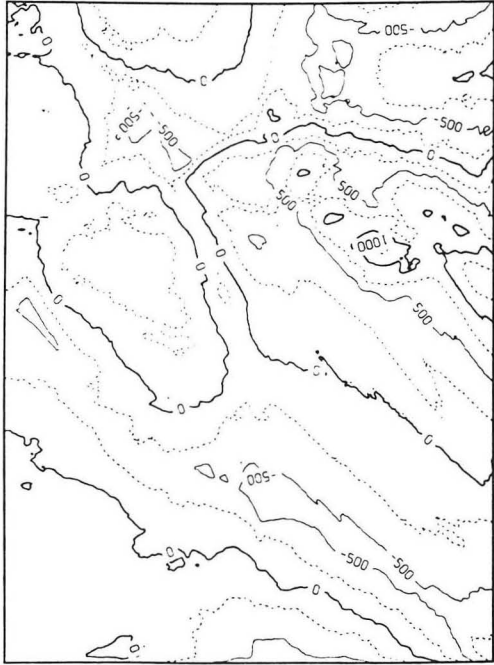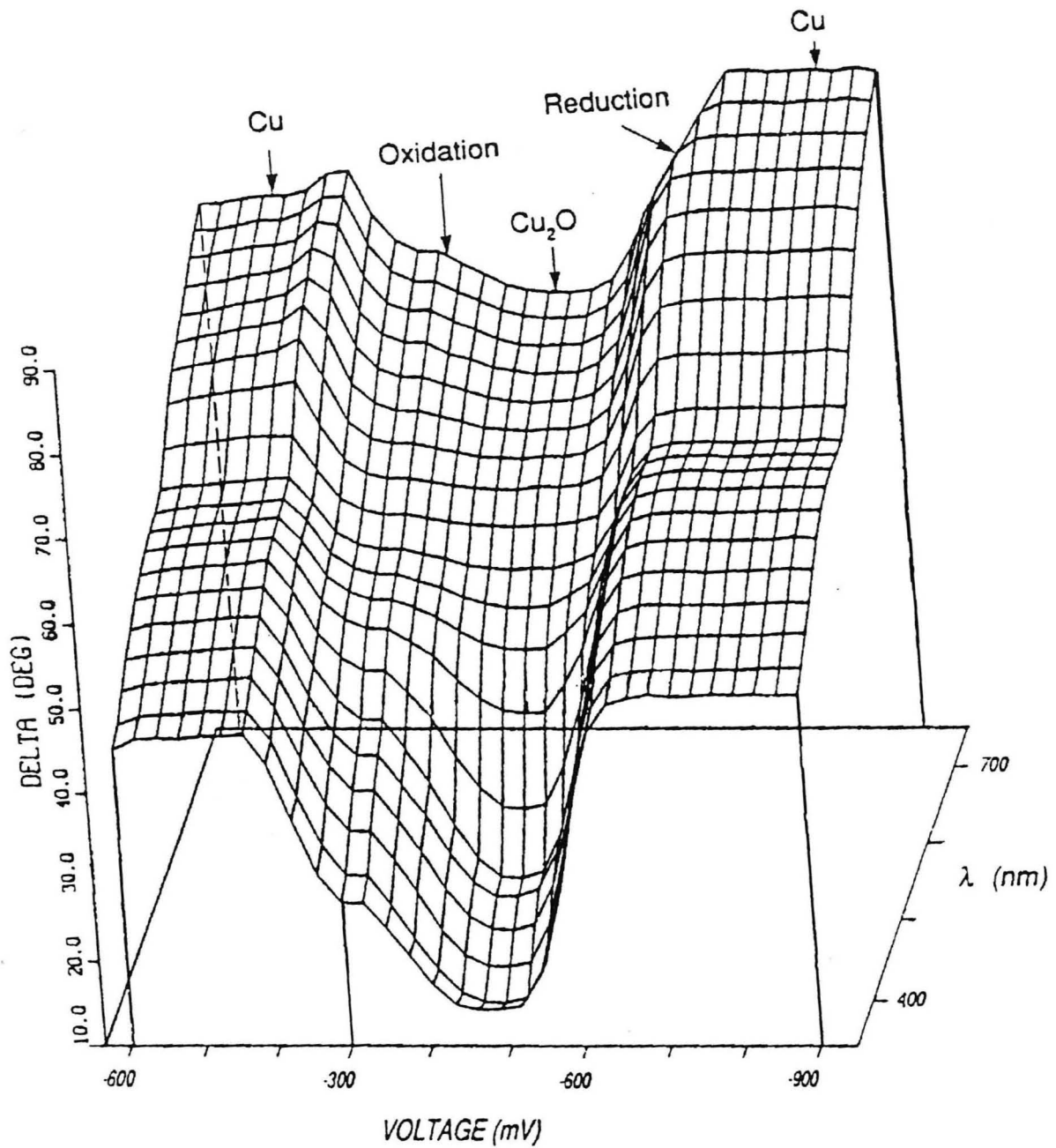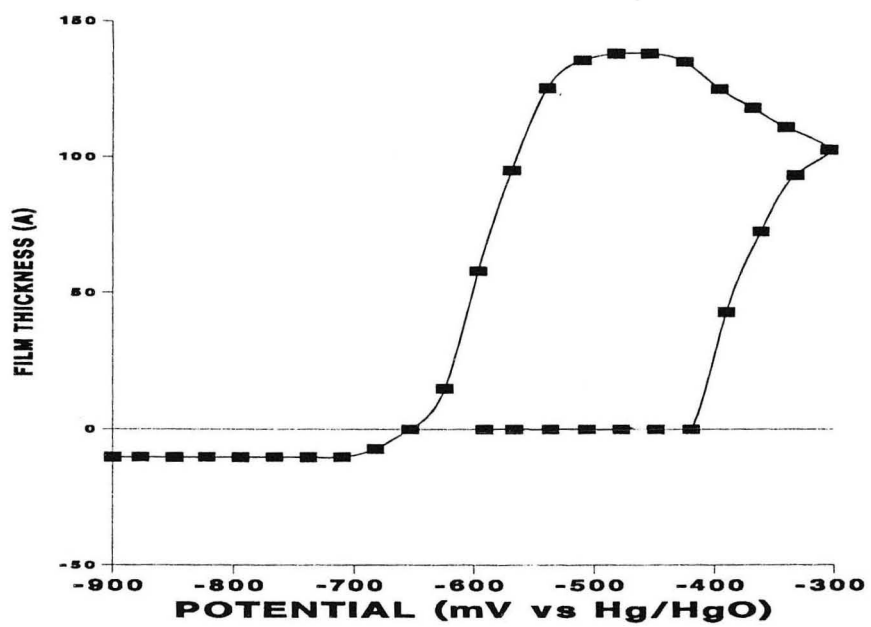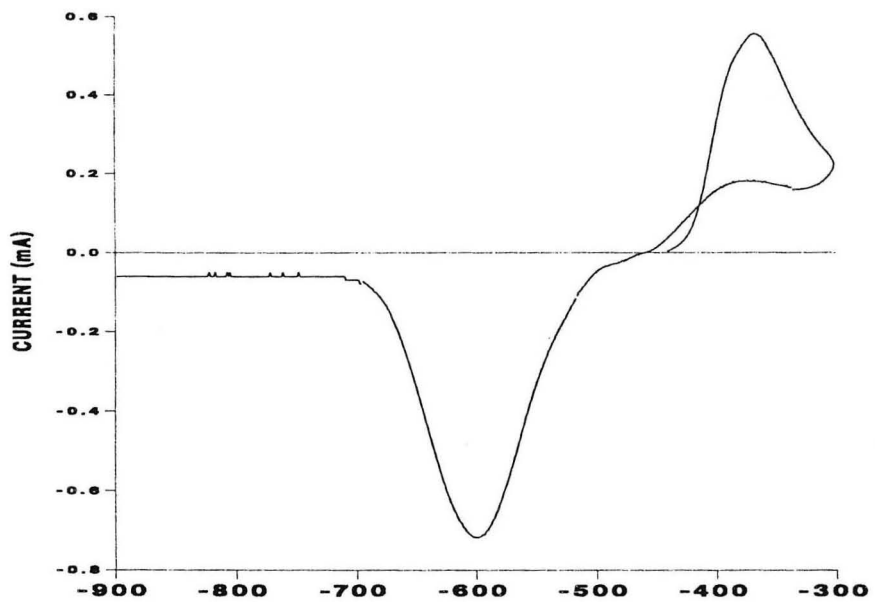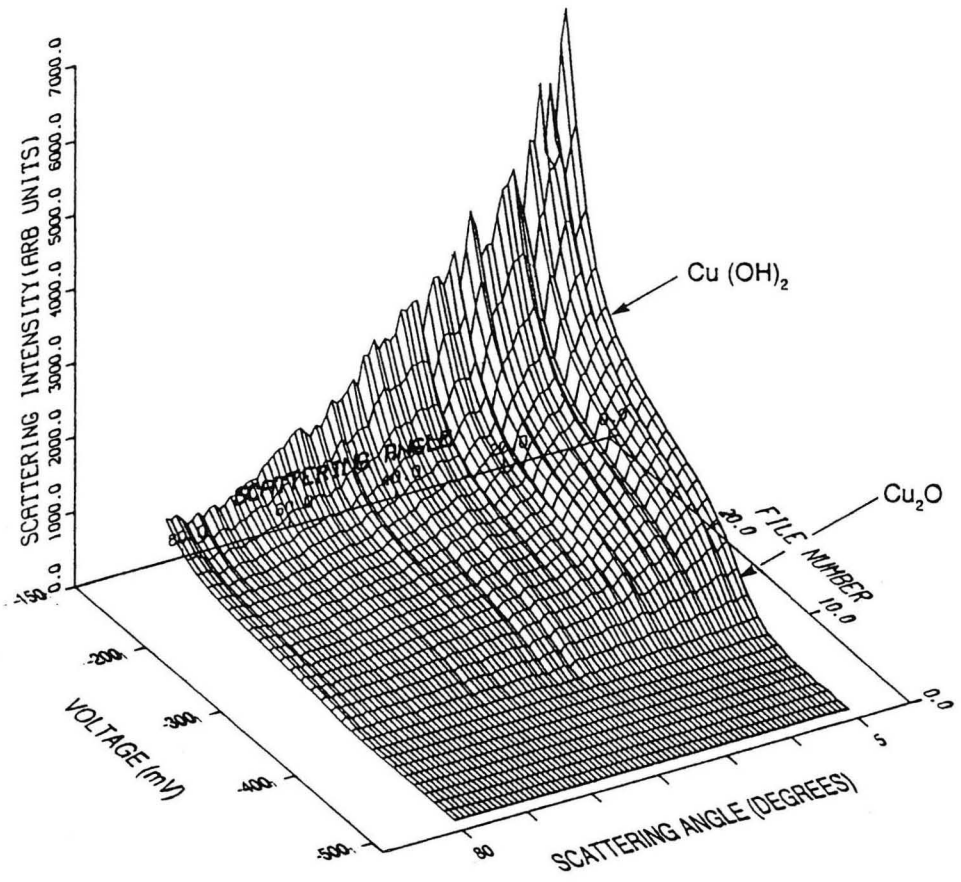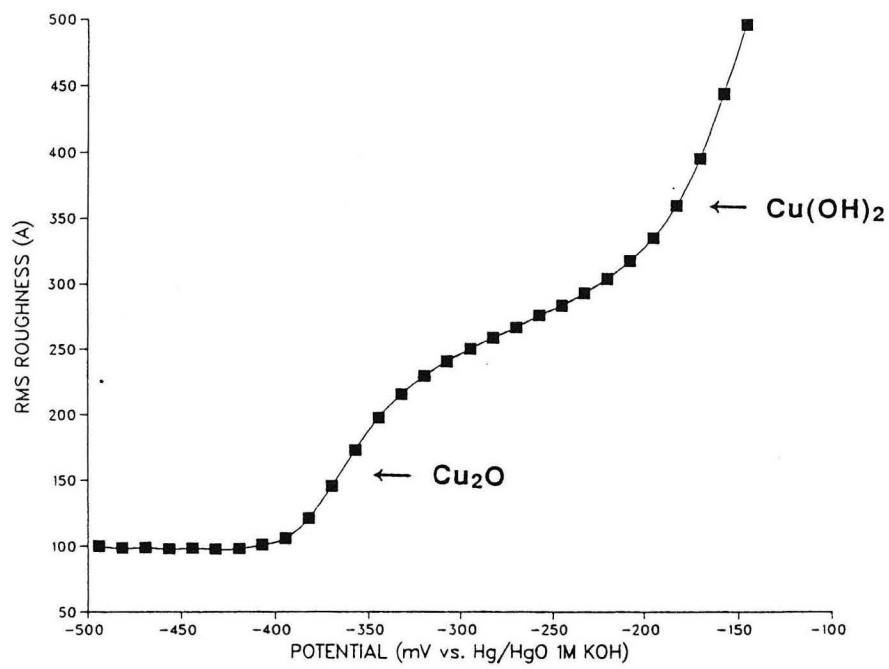
XBL 888-3086A

Fig. 8

XBB 879-8192

Fig. 9

24

Fig. 10

XBL 891-348A

Porous Island Oxide

Non Porous Oxide

Substrate

XBL 865-2106

Fig. 11

26
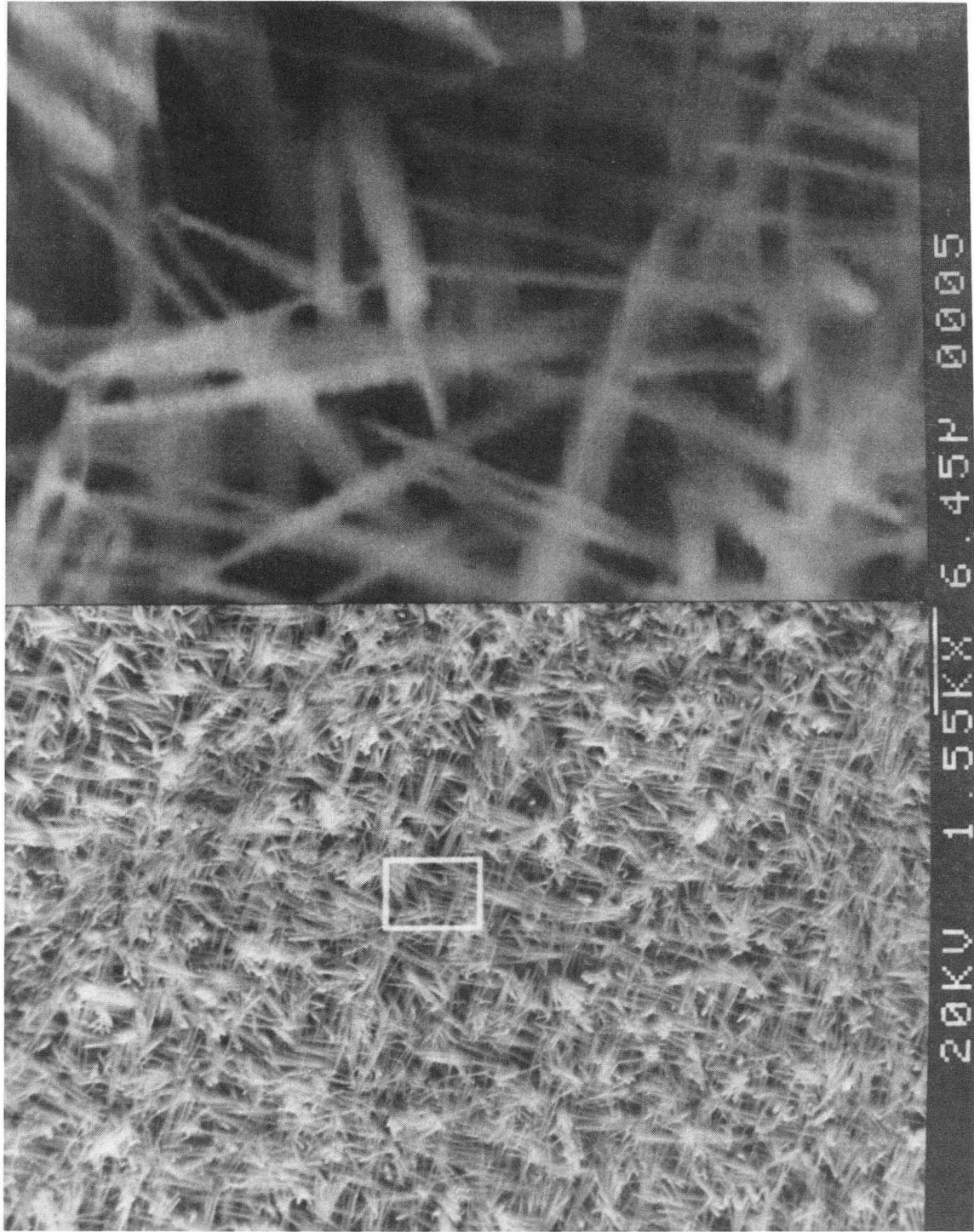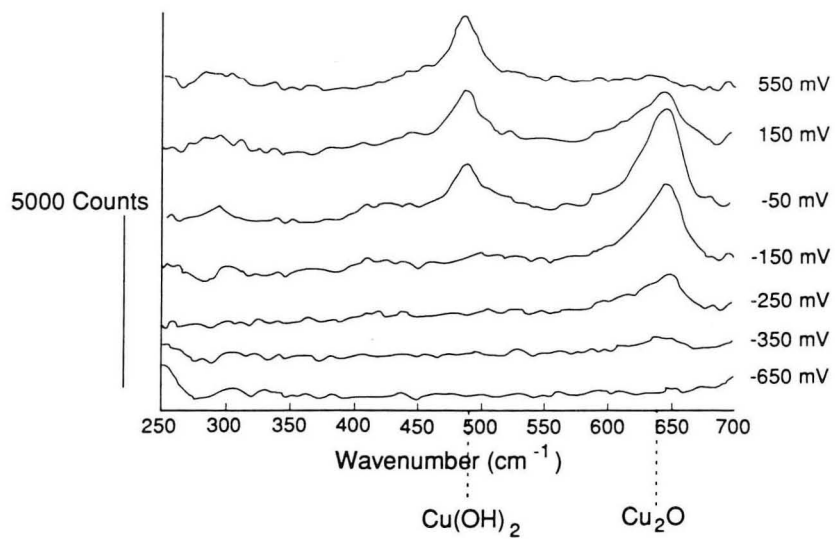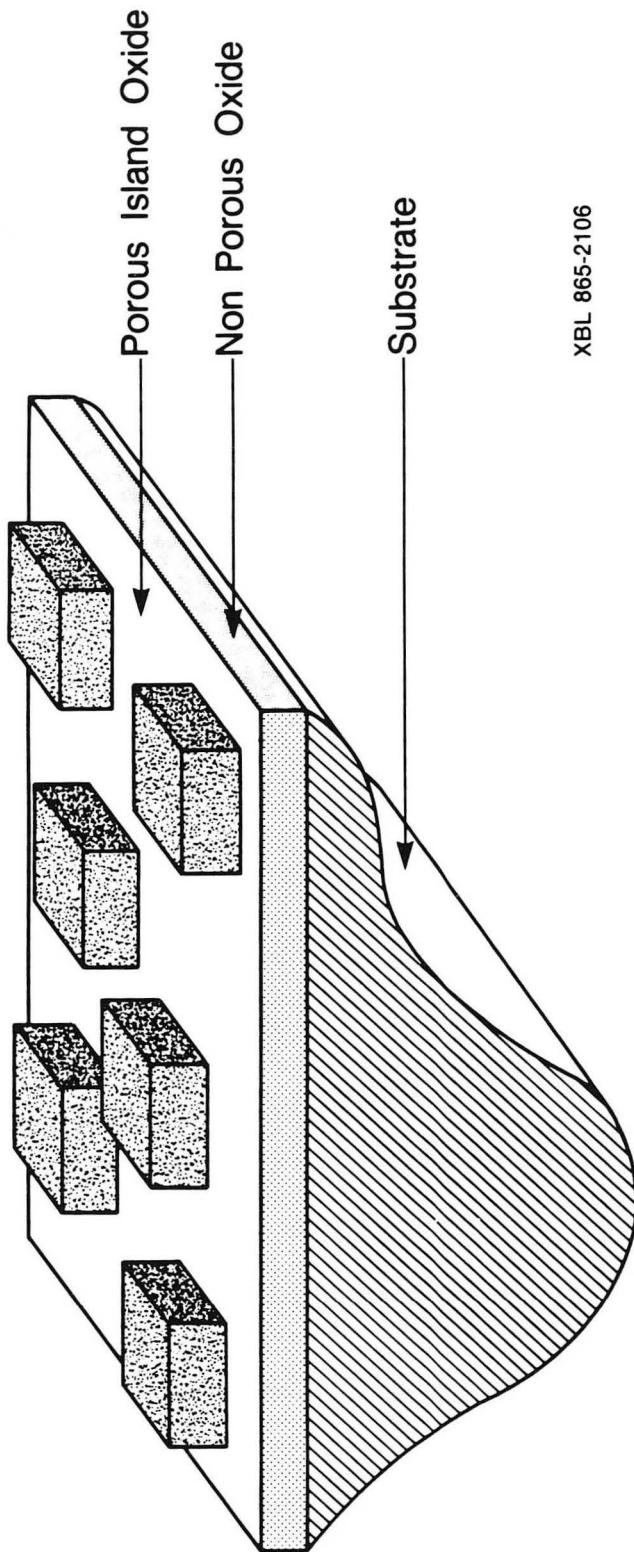
PRIMARY LAYER THICKNESS
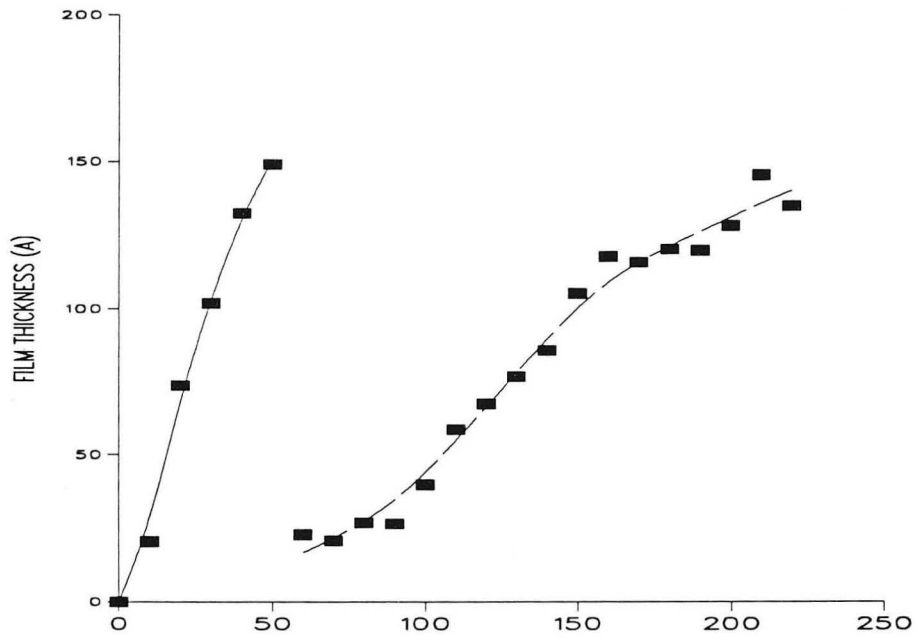
SECONDARY CRYSTAL THICKNESS

XBL 876-3024

Fig. 12

27

XCG 8512-544

Fig. 13

28

SCATTERING INTENSITY(ARB UNITS)

2000.0

1500.0

1000.0

500.0

0.0

SCATTERING ANGLE

80.0

60.0

40.0

TIME (Sec)

120

90

60

30

0

XBL 888-2935

Fig. 14

29

0.25 μ

1 μ

1 μ
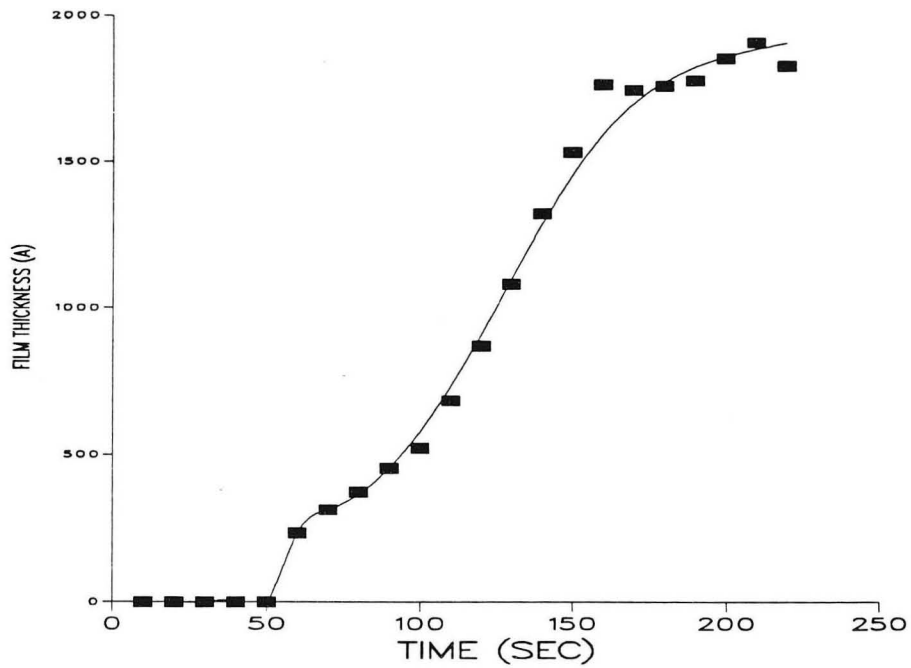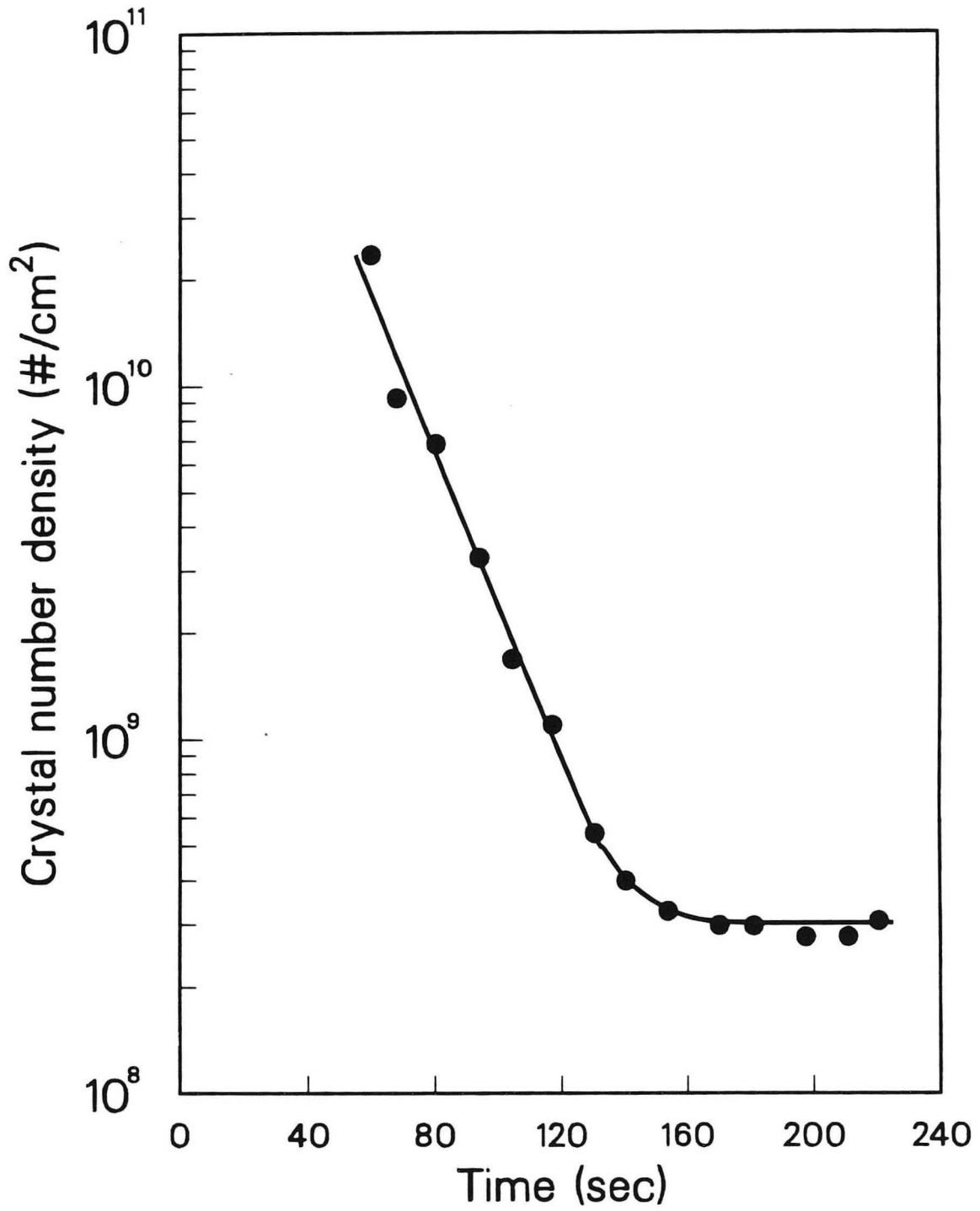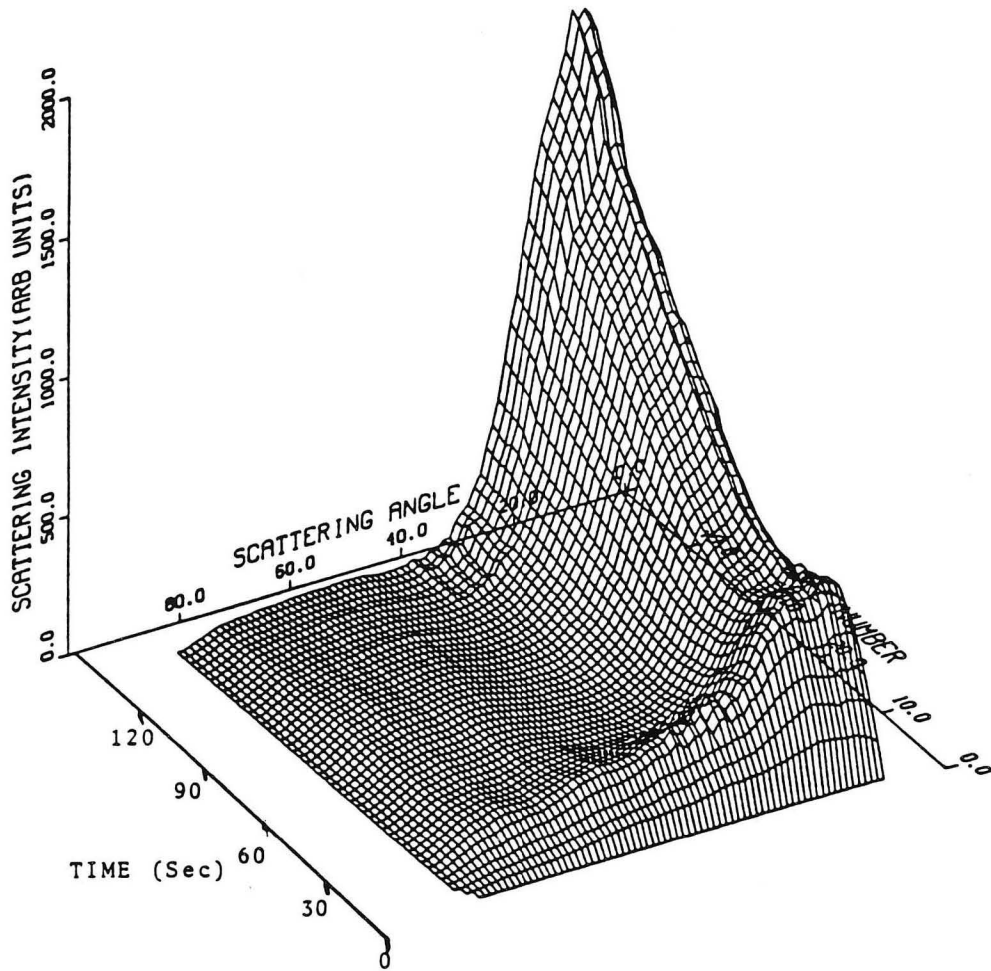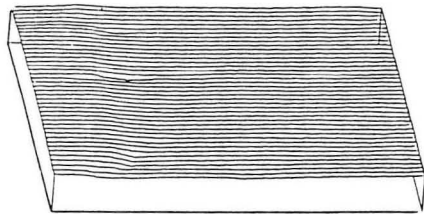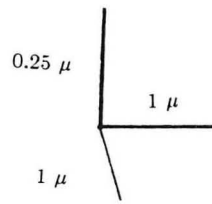
A

Substrate
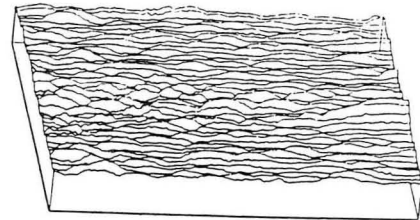
D
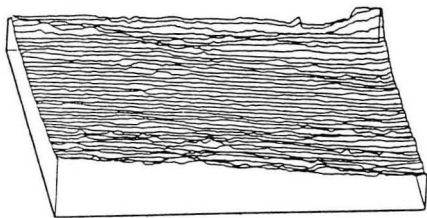
60 seconds

B

30 seconds
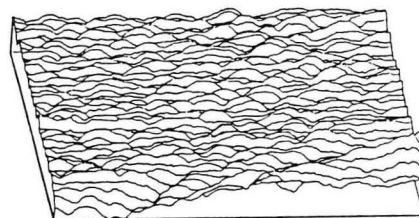
E

75 seconds
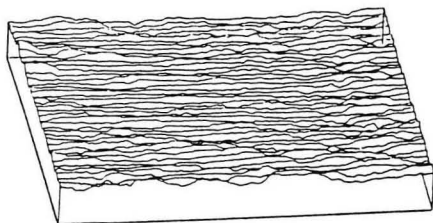
C

45 seconds
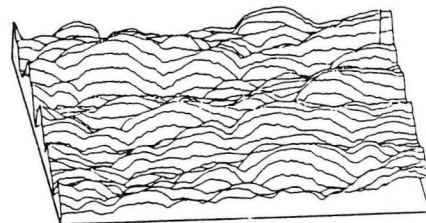
F

120 seconds

XBL 891-85

Fig. 15

XBL 876-3025

Fig. 16

31

1000 Å°

1000 Å°

1000 Å°
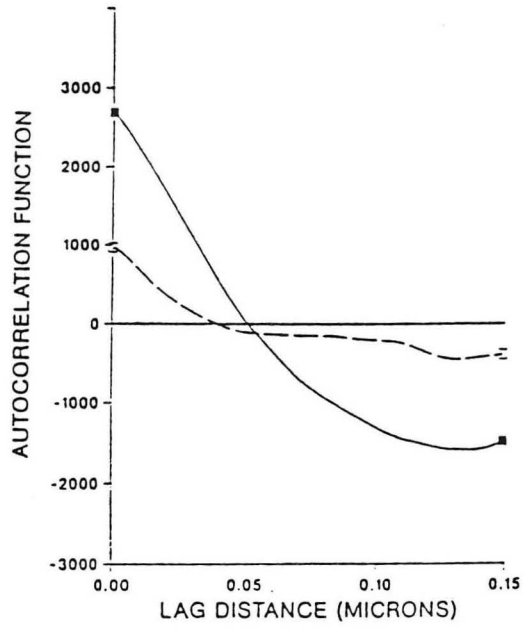
A.

B

C

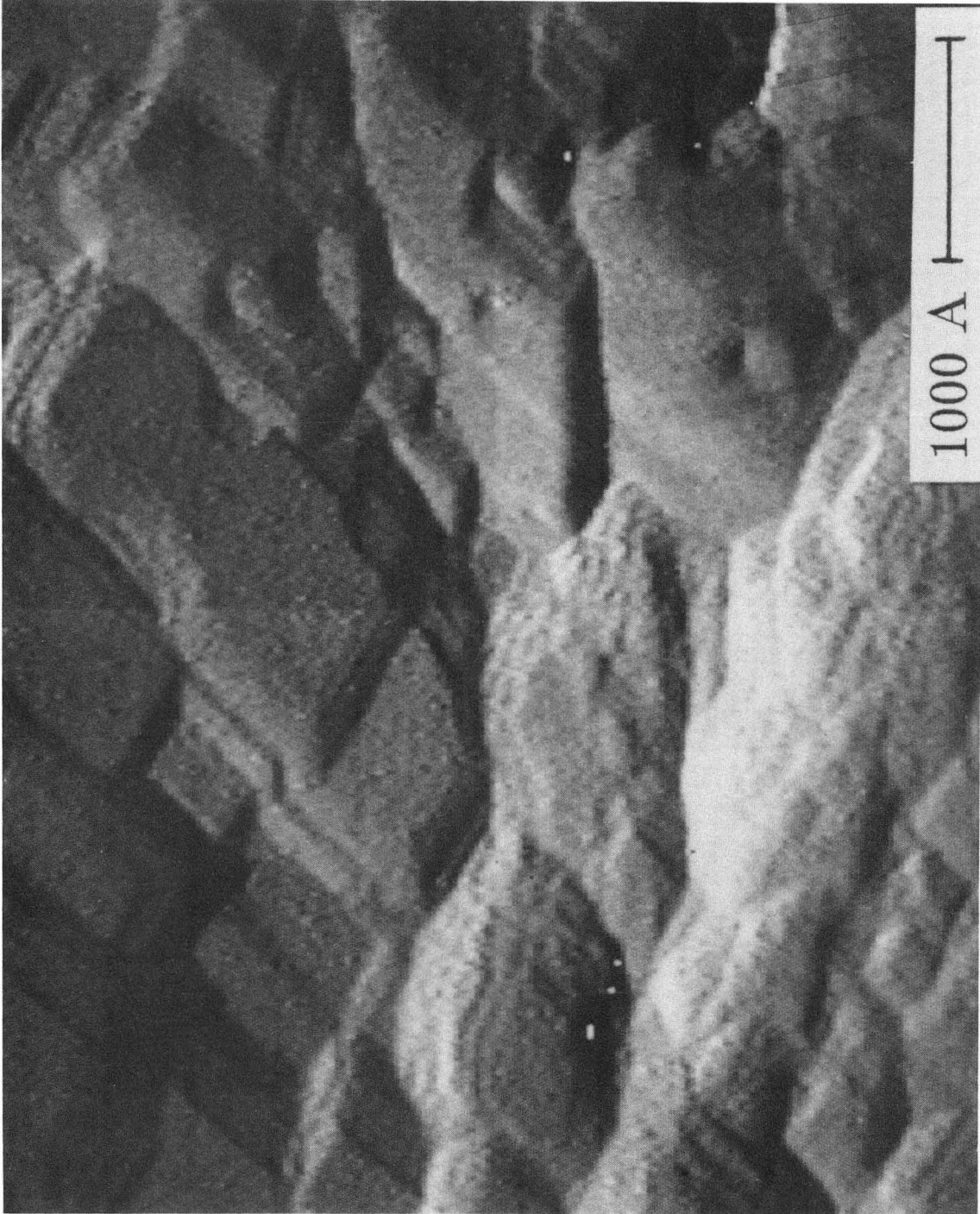D

XBL 891-75

Fig. 17

32
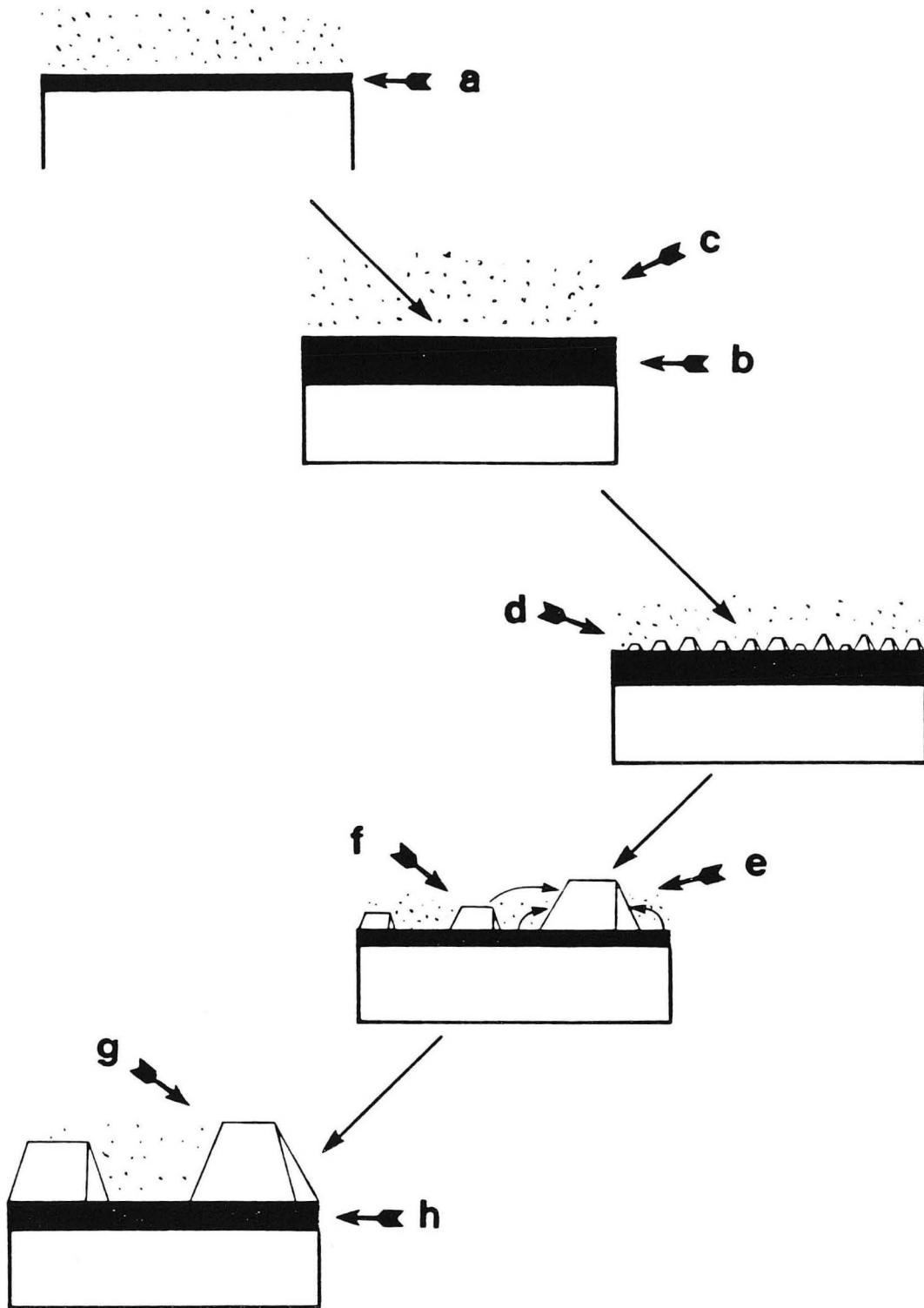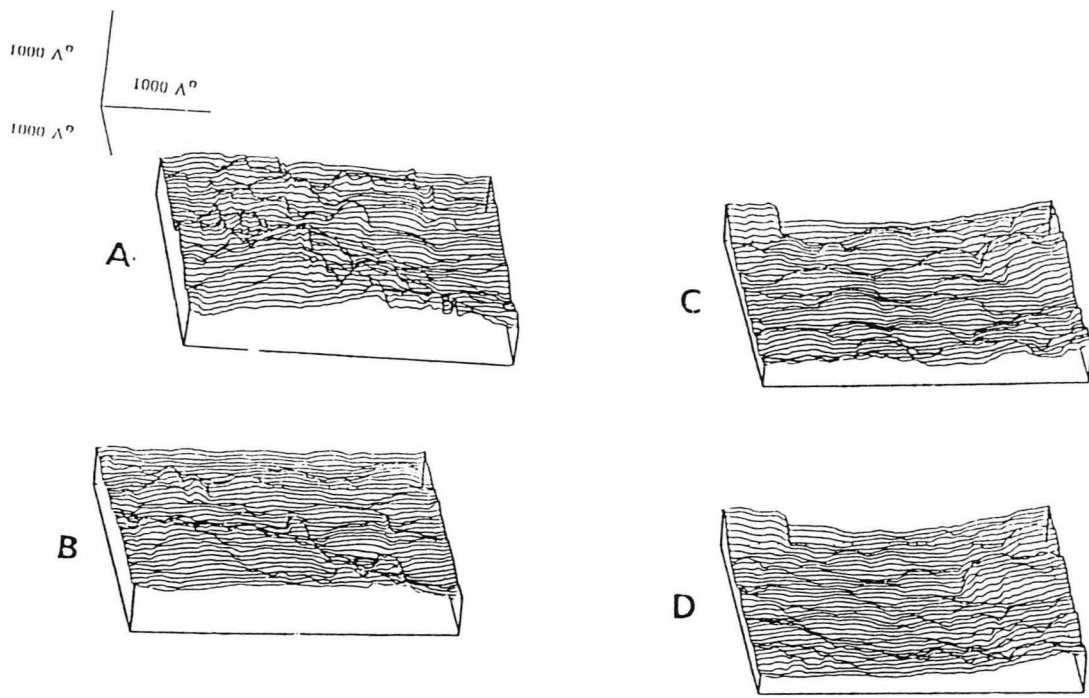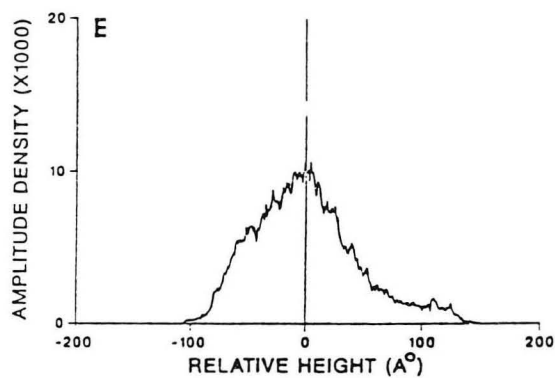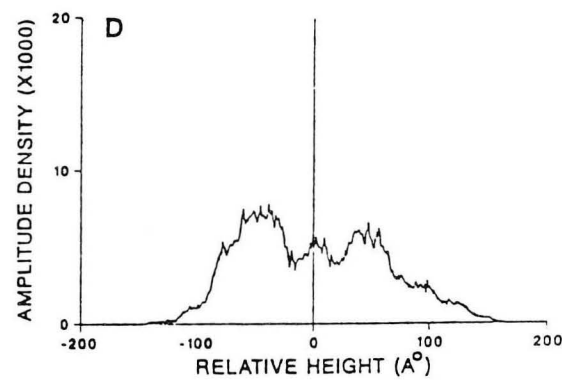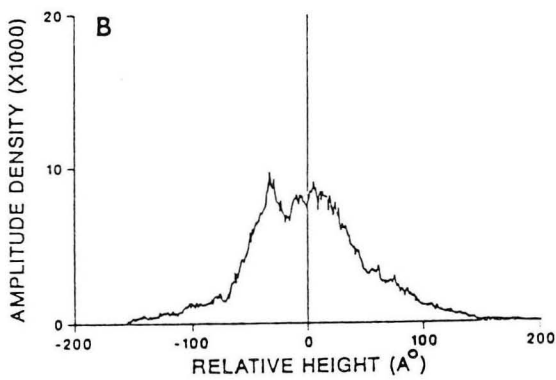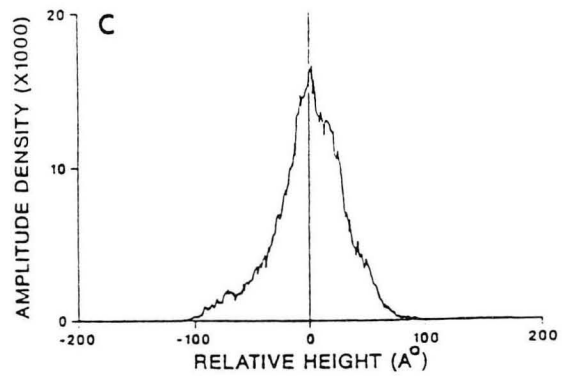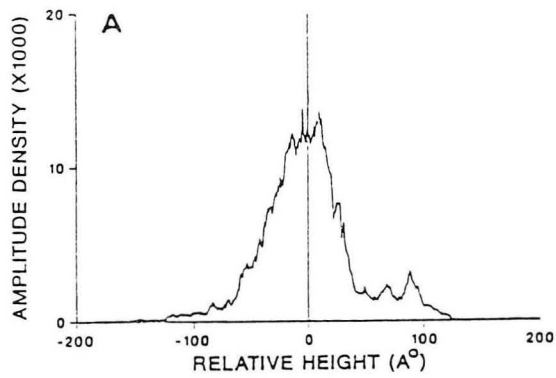
XBL 891-76

Fig. 18

XBL 891-77

Fig. 19

1000 A
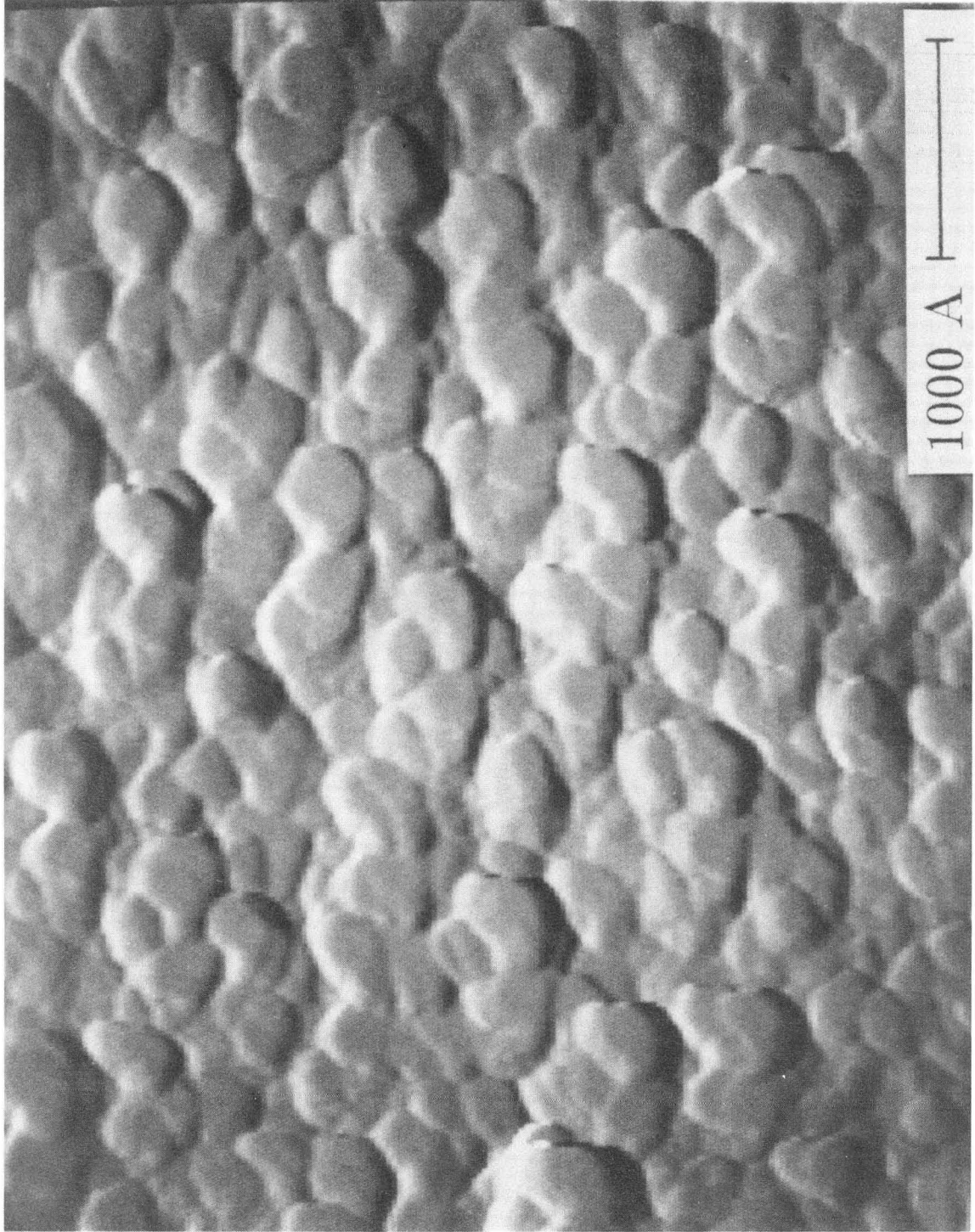
XBB 894-3044

Fig. 20

35

1000 Å

XBB 894-3045

Fig. 21

36

LAWRENCE BERKELEY LABORATORY
UNIVERSITY OF CALIFORNIA
TECHNICAL INFORMATION DEPARTMENT
BERKELEY, CALIFORNIA 94720